Quantum Spin Hall State in Monolayer 1T'-WTe_2

Shujie Tang[1, 2, 3, 4,5†], Chaofan Zhang[1, 2†], Dillon Wong[6], Zahra Pedramrazi[6], Hsin-Zon Tsai[6], Chunjing Jia[1, 2], Brian Moritz[1], Martin Claassen[1], Hyejin Ryu[3, 7, 8], Salman Kahn[6], Juan Jiang[3, 5 ,9], Hao Yan[1, 2], Makoto Hashimoto[11], Donghui Lu[11], Robert G. Moore[1, 2], Chan-Cuk Hwang[9], Choongyu Hwang[8], Zahid Hussain[3], Yulin Chen[10], Miguel M. Ugeda[12,13], Zhi Liu[4,5], Xiaoming Xie[4,5], Thomas P. Devereaux[1, 2], Michael F. Crommie[6,14, 15], Sung-Kwan Mo[3*] & Zhi-Xun Shen[1, 2*]

[1]Stanford Institute for Materials and Energy Sciences, SLAC National Accelerator Laboratory, 2575 Sand Hill Road, Menlo Park, California 94025, USA

[2]Geballe Laboratory for Advanced Materials, Departments of Physics and Applied Physics, Stanford University, Stanford, California 94305, USA

[3]Advanced Light Source, Lawrence Berkeley National Laboratory, Berkeley, California 94720, USA

[4]State Key Laboratory of Functional Materials for Informatics, Shanghai Institute of Microsystem and Information Technology, Chinese Academy of Sciences, Shanghai 200050, China

[5]School of Physical Science and Technology, Shanghai Tech University, Shanghai 200031, China

[6]Department of Physics, University of California at Berkeley, Berkeley, CA 94720, USA

[7]Max Plank POSTECH Center for Complex Phase Materials, POSTECH, Pohang 37673, Korea

[8]Department of Physics, Pusan National University, Busan 46241, Korea

[9]Pohang Accelerator Laboratory, POSTECH, Pohang 37673, Korea

[10]Department of Physics and Clarendon Laboratory, University of Oxford, Parks Road, Oxford, OX1 3PU, UK

[11]Stanford Synchrotron Radiation Lightsource, SLAC National Accelerator Laboratory, 2575 Sand Hill Road, Menlo Park, California 94025, USA

[12]Ikerbasque, Basque Foundation for Science, 48013 Bilbao, Spain

[13]CIC nanoGUNE, 20018 San Sebastián, Spain

[14]Materials Sciences Division, Lawrence Berkeley National Laboratory, Berkeley, California 94720, USA

[15]Kavli Energy Nano Sciences Institute, University of California and Lawrence Berkeley National Laboratory, Berkeley, California 94720, USA

†*These authors contributed equally to this work.*

**To whom correspondence should be addressed: skmo@lbl.gov, zxshen@stanford.edu*

A quantum spin Hall (QSH) insulator is a novel two-dimensional quantum state of matter that features quantized Hall conductance in the absence of magnetic field, resulting from topologically protected dissipationless edge states that bridge the energy gap opened by band inversion and strong spin-orbit coupling[1, 2]. By investigating electronic structure of epitaxially grown monolayer 1T'-WTe_2 using angle-resolved photoemission (ARPES) and first principle calculations, we observe clear signatures of the topological band inversion and the band gap opening, which are the hallmarks of a QSH state. Scanning tunneling microscopy measurements further confirm the correct crystal structure and the existence of a bulk band gap, and provide evidence for a modified electronic structure near the edge that is consistent with the expectations for a QSH insulator. Our results establish monolayer 1T'-WTe_2 as a new class of QSH insulator with large band gap in a robust two-dimensional materials family of transition metal dichalcogenides (TMDCs).

A two-dimensional (2D) topological insulator (TI), or a quantum spin Hall insulator, is characterized by an insulating bulk and a conductive helical edge state, in which carriers with different spins counter-propagate to realize a geometry-independent edge conductance $2e^2/h$ [1, 2]. The only scattering channel for such helical edge current is back scattering, which is prohibited by time reversal symmetry, making QSH insulators a promising material candidate for spintronic and other applications.

The prediction of the QSH effect in HgTe quantum wells sparked the intense research efforts to realize the QSH state [3, 4, 5, 6, 7, 8, 9, 10, 11]. So far only a handful of QSH systems have been fabricated, mostly limited to quantum well structures of three-dimensional(3D) semiconductors such as HgTe/CdTe [3] and InAs/GaSb [6]. Edge conduction consistent with a QSH state has been observed [3, 6, 12]. However, the behavior under the magnetic field, where the time reversal

symmetry is broken, cannot be explained within our current understanding of the QSH effect [13, 14]. There have been continued efforts to predict and investigate other material systems to further advance the understanding of this novel quantum phenomenon [5, 7, 8, 9, 15]. So far, it has been difficult to make a robust 2D material with QSH state, a platform needed for wide-spread study and application. The small band gaps exhibited by many candidate systems as well as their vulnerability to strain, chemical adsorption, and element substitution make them impractical for the advanced spectroscopic studies or applications. For example, a QSH insulator candidate stanene, a monolayer analog of graphene for tin, grown on Bi_2Se_3 becomes topologically trivial due to the modification of its band structure by the underlying substrate [11, 16]. The free standing Bi film with 2D bonding on a cleaved surface has shown edge conduction [9], but its topological nature is still debated [17]. It takes 3D out-of-plane bonding with the substrate and large strain (up to 18%) to open a bulk energy gap in monolayer bismuth [15]. Such 3D bonding structure may induce similar surface issues as seen in 3D semiconductor QSH systems. Monolayer FeSe grown on a $SrTiO_3$ substrate has also emerged as a model system to support both QSH and superconductivity. However, due to doping from the substrate the Fermi energy (E_F) is more than 500meV higher than the nontrivial gap, making it less practical for applications[18].

1T' phase monolayer TMDCs MX_2, M = (W, Mo) and X = (Te, Se, S), are theoretically predicted to be a promising new class of QSH insulators with large band gap [10]. Among them, WTe_2 is the only one for which the 1T' phase is most energetically favored. Realization of a QSH insulator in 2D TMDCs would be a breakthrough as this is a robust family of materials with none of the complications from surface/interface dangling bonds that are seen in 3D semiconductors, enabling a broad range of study and application of QSH physics. In this work, we report a successful growth of monolayer 1T'-WTe_2 using molecular beam epitaxy (MBE) on

a bilayer graphene (BLG) substrate. In-situ ARPES measurements clearly show the band inversion and the opening of a 55meV bulk band gap, which is an order of magnitude larger than gaps seen in quantum wells of 3D semiconductors [3, 6]. Scanning tunneling spectroscopy (STS) spectra show evidence of the insulating bulk and conductive edge nature of 1T'-WTe_2. Our results thus provide compelling experimental evidences of a QSH insulator phase in monolayer 1T'-WTe_2.

Figure 1a presents the crystal structure of monolayer 1T'-WTe_2. MX_2 has three typical phases, namely 2H, 1T and 1T'. 1T-WTe_2 is composed of three hexagonally packed atomic layers in an ABC stacking. The metal atoms are in octahedral coordination with the chalcogen atoms. This is not a stable phase in freestanding form and undergoes a spontaneous lattice distortion into the 1T' phase via a doubling of the periodicity in the X direction. W atoms are dislocated from the original octahedral positions to form a zigzag chain in the Y direction.

The lattice distortion from the 1T phase to the 1T' phase induces band inversion and causes 1T'-WTe_2 to become topologically non-trivial [10, 19, 20]. Fig. 1b schematically summarizes this topological phase transition in 1T'-WTe_2. Without spin-orbit coupling (SOC), the inverted bands cross at a momentum point along the Γ-Y direction, forming a Dirac cone. Strong SOC lifts the degeneracy at the Dirac point, opening a bulk band gap. Following the bulk boundary correspondence [21, 22], the helical edge state is guaranteed by the gapped topologically non-trivial bulk band structure.

Our first-principles band structure calculations for 1T- and 1T'-WTe_2 are presented in Figs. 1c- e, which is generally consistent with the literature[10, 20, 23]. The key bands for the band inversion with opposite parities are marked to track their evolution. In 1T-WTe_2, the bands from $5d_{xz}$ and $5d_{z^2}$ orbitals of W are separated by the E_F (Fig. 1c). Due to the symmetry breaking

105 through the lattice distortion from 1T to 1T', these orbitals hybridize substantially. Fig. 1d shows
106 that the d_{z^2} orbital is lowered below E_F whereas the d_{xz} orbital lifts in the opposite direction near
107 the Γ point. Because these two inverted bands have different parity at the Γ point, the Z_2
108 invariant *v*, in which $(-1)^v$ determined by the product of all occupied band parity eigenvalues [24],
109 changes from 0 to 1. The valence band maximum in 1T' phase is mainly from W d_{yz} orbital, with
110 an even parity at the Γ point. When its degeneracy with d_{xz} orbital in 1T phase is lifted by the
111 lattice distortion, the band stays below E_F and does not involve in the band inversion. With the
112 inclusion of SOC (Fig. 1e), the bands further hybridize with each other and the degeneracies at
113 the Dirac cones formed by the band inversion are lifted, opening a band gap in the bulk states.
114 We note here that different calculation methods give different estimates on the size of the band
115 gap for strain-free 1T'-WTe_2 monolayers. The generalized-gradient approximation (PBE) usually
116 underestimates the bandgap and gives a negative band gap value[10], while PBE with hybrid
117 function (HSE06) gives a positive value [23].

118 Figure 2 summarizes the MBE growth and the characterization of 1T'-WTe_2 on
119 BLG/SiC(0001) (See Methods for the details of the growth condition). The reflection high-
120 energy electron diffraction (RHEED) pattern of the BLG substrate and the monolayer 1T'-WTe_2
121 are presented in Fig. 2a. Clean vertical line profiles after the deposition of W and Te clearly
122 indicate the layer-by-layer growth mode. Using the lattice constant of BLG (a=2.46 Å) as a
123 reference, the lattice constant of the grown film is estimated to be ~ 6.3Å ± 0.2 Å, consistent
124 with the expected value for monolayer 1T'-WTe_2 [23]. The angle-integrated core level
125 photoemission spectrum (Fig. 2b) exhibits the characteristic peaks of W and Te for the 1T'
126 phase. Two differently coordinated types of Te contribute two sets of Te *4d* peaks, while the
127 clean doublet feature of the W *4f* peaks indicates a pure 1T' phase rather than a mixed phase of

1T' and 1H [25]. Fig. 2c is an atomically resolved scanning tunneling microscopy (STM) image of 1T'-WTe_2, from which a ~7.5° angle distortion is observed, which is universal in bulk 1T' phase MX_2 [25, 26]. Figs. S5a and b show a typical morphology of the 1T'-WTe_2 on bilayer graphene substrate. A typical diameter for a branched island is ~ 50 nm, with branches having sizes larger than 20 nm x 20 nm. Since the growth is edge-diffusion limited, the edge geometry is random.

The measured Fermi surface (FS) from the in-situ ARPES is shown in Fig. 2e. Due to the symmetry mismatch between the two-fold rotational symmetry of the sample and the three-fold symmetry of the substrate, there exist three energetically equivalent domains rotated by 120 degrees with respect to each other and each domain contributes two electron pockets along the ΓY direction of their respective BZs [27]. The experimental band dispersion along ΓY cutting the FS electron pockets is inevitably superposed with the contributions from ΓP and ΓP'. However, as shown in Fig. 2f - h, the valence bands from ΓP' and ΓP directions are enclosed by the ΓY band. Therefore, the existence of the multiple domains does not affect the characterization of the gap size and the separation between valence and conduction bands. Overall band structure measured with ARPES (Figs. 2f & g) gives a nice agreement with the HSE06 calculation (Fig. 2g), demonstrating the 1T' nature and the high quality of our thin film samples. The predicted band inversion in 1T'-WTe_2 is well established experimentally by a polarization-dependent ARPES measurement, from which one can clearly distinguish in- and out-of-plane orbital characters and their inversion around the Γ point (Supplementary Figs. S1 and S2). This indicates the nontrivial topology of the 1T'-WTe_2.

The signature of strong SOC in 1T'-WTe_2 is the lifting of state degeneracy at the Dirac cones along the ΓY direction, resulting in an opening of the bulk gap as illustrated in Fig. 3a. This can be seen more clearly in the energy distribution curves (EDCs) extracted at the valence band top

and the conduction band bottom. Since ARPES data in Fig. 2 only show faint tails of the bulk conduction band, we deposited potassium (K) onto the surface to raise E_F [28] and make the conduction band more clearly visible to ARPES. Fig. 3b focuses only the low energy electronic structure of surface K-doped 1T'-WTe_2, with E_F raised ~ 70meV to reveal the conduction band bottom more clearly. The corresponding EDCs in Fig. 3c show that the conduction band and the valence band are well separated from each other. To quantify the size of the band gap, we extracted two EDCs from the momentum positions at the conduction band bottom and valence band top, labeled by the dashed lines in Fig. 3b, and we overlaid them in Fig. 3d. The red and green peaks in Fig. 3d corresponds to the energy positions of the conduction band bottom and the valence band top, respectively. We estimate the size of the band gap to be 55 ± 20meV and 45 ± 20meV in intrinsic and K-doped samples, respectively (Supplementary Fig. S3). This is in clear contrast to the bulk 1T'-WTe_2, which is a semimetal with a complex band structure near E_F exhibiting multiple Fermi pockets [29]. The stacking of energy momentum dispersions with fine momentum steps parallel to the ΓY direction (Figs. 3e and 3f) further establish the effect of SOC by showing that the gap never closes for any momentum across the FS.

Now that we have established the band inversion and the opening of a band gap due to the strong SOC, the remaining signature of a QSH insulator is the conductive edge state in contrast to the insulating bulk, which can be better examined by STS. Fig. 4a shows the local differential conductance (dI/dV) spectrum taken at a point far away from the WTe_2 edges, which represents the bulk local density of states (LDOS). The peak positions in dI/dV are in good agreement with the band edges found in ARPES. The agreement between ARPES and STS further extends to the size of the gap, as the mean gap size determined by STS is 56 ± 14 meV (Supplementary Figs. S6). In contrast to the gap in the bulk, dI/dV at a 1T'-WTe_2 edge is quite different, showing a

174 "V-shape" spectrum with states filling in the bulk gap (Fig. 4b), which may indicate the
175 existence of a conductive edge state. Indeed, similar dI/dV spectral line shapes have been
176 reported for other topological systems with distinct edge states [15, 30] and have been attributed to
177 the one-dimensional (1D) nature of the edge states and the emergence of a Luttinger liquid [15].
178 Fig. 4c shows dI/dV as a function of energy and distance away from an edge, which
179 demonstrates that the V-shaped conductance is localized at the edge of the WTe_2. We observe
180 that such localized edge states run continuously along our sample edges (Supplementary Figs.
181 S7), with only small variations in the fine details of the spectra, regardless of the size, shape, and
182 edge-roughness of samples. This provides evidence of the edge state's topologically non-trivial
183 nature. [30, 31]

184 By combining ARPES and STS results, we provide strong evidence supporting the direct
185 observation of all the characteristic electronic properties of the a QSH state with large energy
186 gap in 1T'-WTe_2, confirming the theoretical prediction [10]. Such a robust platform for QSH
187 insulator in 2D TMDCs should provide new opportunities for fundamental studies and novel
188 device applications. Since TMDCs are inert, widely available, can be exfoliated for transport
189 experiments, and be made into few-layer and van der Waals heterostructure devices, we expect
190 them to be the material of choice for much expanded, multimodal effort to understand and utilize
191 QSH systems.

192

193 ## Methods

194 **Thin film growth.** The monolayer 1T'-WTe_2 films were grown by MBE on bilayer graphene
195 (BLG) epitaxially grown on 6H-SiC[32]. Growth was performed at Beamline 10.0.1, Advanced

Light Source, Lawrence Berkeley National Laboratory. The base pressure of MBE chamber was ~ 4×10^{-10} Torr. Ultrahigh purity tellurium (99.999%) and tungsten (99.999%) was evaporated from an effusion cell and an electron beam evaporator, respectively. The flux ratio between tungsten and tellurium is set between 1:10~1:20. We found that the quality of sample doesn't depend much on the ratio. However, it critically depends on the substrate temperature. The substrate temperature was held at 280 ^{o}C during growth. The growth process was monitored by RHEED. The growth rate was ~ 40 min per monolayer. After growth we annealed the sample at 300 ^{o}C for 2 hours to improve the film quality. [33]

ARPES measurement. In-situ ARPES measurements were performed at Beamline 10.0.1, Advanced Light Source, Lawrence Berkeley National Laboratory. ARPES data were acquired with Scienta R4000 electron analyzer at a temperature of 60 K. The energy and angular resolutions are set to be 18meV and 0.1^{o}, respectively. Two different photon polarizations were used. In S-polarization, the electric field of the photon is perpendicular to the incidence plane defined by the sample normal and the photon momentum. In P-polarization, the photon electric field is 10^{o} out of the incidence plane. It is composed of both *s* polarized and *p* polarized light. The intensity ratio between *s* polarization and *p* polarization is 17:83. We nonetheless refer to this as P-polarization, since the actual polarization is dominated by *p* polarized light. The spot size of the photon beam on the sample was ~100μm × 100μm. The potassium used to perform a surface doping of the film was evaporated from a SAES Getters alkali metal dispenser.

STM measurement. To protect the film from an exposure to air during the transfer to the STM chamber, Te and Se capping layers with thicknesses of ~100nm were both deposited on the film (Te layer first) before taking the samples out of the UHV system of Beamline 10.0.1. Annealing at 200 ^{o}C for half an hour was enough to remove the capping layer right before STM

measurements after having introduced the sample into the STM UHV system. Scanning tunneling spectroscopy (STS) measurements were performed at T = 4.8 K with platinum iridium tips calibrated against the Au(111) Shockley surface state. dI/dV measurements were obtained via lock-in detection of the a.c. tunneling current induced by a 5 mV, 613.7 Hz modulation voltage applied to the STM tip.

Electronic structure calculations. The band structure and orbital content as presented in Fig. 1 are calculated using full-potential linearized augmented plane wave method implemented in Wien2k. *Ab initio* calculations were performed in the framework of the Perdew-Burke-Ernzerhof (PBE) type generalized gradient approximation (GGA) of density functional theory (DFT). The band structure calculation as presented in Fig. 2g, h and Fig. 3a in the main text were calculated using VASP package with projector augmented wave pseudo-potentials, using Heyd-Scuseria-Ernzerhof (HSE06) exchange-correlation functional with spin-orbital coupling (SOC). The lattice constants and internal atom positions are optimized with PBE exchange-correlation functional[10].

Data Availability. The data that support the plots within this paper and other findings of this study are available from the corresponding author upon reasonable request.

References

1. Kane, C. L. & Mele, E. J. Quantum Spin Hall Effect in Graphene. *Phys. Rev. Lett.* **95**, 226801 (2005).

2. Bernevig, B. A., Hughes, T. L. & Zhang, S.-C. Quantum Spin Hall Effect and Topological Phase Transition in HgTe Quantum Wells. *Science* **314**, 1757-1761 (2006).

3. König, M.*, et al.* Quantum Spin Hall Insulator State in HgTe Quantum Wells. *Science* **318**, 766-770 (2007).

4. Liu, C., *et al.* Quantum Spin Hall Effect in Inverted Type-II Semiconductors. *Phys. Rev. Lett.* **100**, 236601 (2008).

5. Liu, Z., *et al.* Stable Nontrivial Z_2 Topology in Ultrathin Bi (111) Films: A First-Principles Study. *Phys. Rev. Lett.* **107**, 136805 (2011).

6. Knez, I., Du, R.-R. & Sullivan, G. Evidence for Helical Edge Modes in Inverted InAs/GaSb Quantum Wells. *Phys. Rev. Lett.* **107**, 136603 (2011).

7. Xu, Y., *et al.* Large-Gap Quantum Spin Hall Insulators in Tin Films. *Phys. Rev. Lett.* **111**, 136804 (2013).

8. Weng, H., Dai, X. & Fang, Z. Transition-Metal Pentatelluride $ZrTe_5$ and $HfTe_5$: A Paradigm for Large-Gap Quantum Spin Hall Insulators. *Phy. Rev. X* **4**, 011002 (2014).

9. Drozdov, I. K., *et al.* One-dimensional topological edge states of bismuth bilayers. *Nat. Phys.* **10**, 664-669 (2014).

10. Qian, X., Liu, J., Fu, L. & Li, J. Quantum spin Hall effect in two-dimensional transition metal dichalcogenides. *Science* **346**, 1344-1347 (2014).

11. Zhu, F.-F., *et al.* Epitaxial growth of two-dimensional stanene. *Nat. Mater.* **14**, 1020-1025 (2015).

12. Nowack, K. C., *et al.* Imaging currents in HgTe quantum wells in the quantum spin Hall regime. *Nat. Mater.* **12**, 787-791 (2013).

13. Ma, E. Y., *et al.* Unexpected edge conduction in mercury telluride quantum wells under broken time-reversal symmetry. *Nat. Commun.* **6**, 7252 (2015).

14. Fabrizio, N., *et al.* Edge transport in the trivial phase of InAs/GaSb. *New. J. Phys.* **18**, 083005 (2016).

15. Reis, F., *et al.* Bismuthene on a SiC Substrate: A Candidate for a New High-Temperature Quantum Spin Hall Paradigm. Preprint at http://adsabs.harvard.edu/abs/2016arXiv160800812R (2016).

16. Xu, Y., Tang, P. & Zhang, S.-C. Large-gap quantum spin Hall states in decorated stanene grown on a substrate. *Phys. Rev. B* **92**, 081112 (2015).

17. Takayama, A., *et al.* One-Dimensional Edge States with Giant Spin Splitting in a Bismuth Thin Film. *Phys. Rev. Lett.* **114**, 066402 (2015).

18. Wang, Z. F., *et al.* Topological edge states in a high-temperature superconductor FeSe/SrTiO3(001) film. *Nat. Mater.* **15**, 968-973 (2016).

19. Keum, D. H., *et al.* Bandgap opening in few-layered monoclinic $MoTe_2$. *Nat. Phys.* **11**, 482-486 (2015).

20. Choe, D.-H., Sung, H.-J. & Chang, K. J. Understanding topological phase transition in monolayer transition metal dichalcogenides. *Phys. Rev. B* **93**, 125109 (2016).

21. Essin, A. M. & Gurarie, V. Bulk-boundary correspondence of topological insulators from their respective Green's functions. *Phys. Rev. B* **84**, 125132 (2011).

22. Hasan, M. Z. & Kane, C. L. *Colloquium*: Topological insulators. *Rev. Mod. Phys.* **82**, 3045-3067 (2010).

23. Zheng, F., *et al.* On the Quantum Spin Hall Gap of Monolayer 1T'-WTe_2. *Adv. Mater.* **28**, 4845-4851 (2016).

24. Fu, L. & Kane, C. L. Topological insulators with inversion symmetry. *Phys. Rev. B* **76**, 045302 (2007).

25. Das, P. K., *et al.* Layer-dependent quantum cooperation of electron and hole states in the anomalous semimetal WTe_2. *Nat. Commun.* **7**, 10847 (2016).

26. Hla, S. W., Marinković, V., Prodan, A. & Muševič, I. Proceedings of the 15th European Conference on Surface ScienceSTM/AFM investigations of β-$MoTe_2$, α-$MoTe_2$ and WTe_2. *Surf Sci.* **352**, 105-111 (1996).

27. Ugeda, M. M., *et al.* Characterization of collective ground states in single-layer $NbSe_2$. *Nat. Phys.* **12**, 92-97 (2016).

28. Zhang, Y., *et al.* Direct observation of the transition from indirect to direct bandgap in atomically thin epitaxial $MoSe_2$. *Nat. Nanotech.* **9**, 111-115 (2014).

29. Jiang, J., *et al.* Signature of Strong Spin-Orbital Coupling in the Large Nonsaturating Magnetoresistance Material WTe_2. *Phys. Rev. Lett.* **115**, 166601 (2015).

30. Pauly, C., *et al.* Subnanometre-wide electron channels protected by topology. *Nat. Phys.* **11**, 338-343 (2015).

31. Lin, H., *et al.* Topological Dangling Bonds with Large Spin Splitting and Enhanced Spin Polarization on the Surfaces of Bi2Se3. *Nano. Lett.* **13**, 1915-1919 (2013).

32. Qingyan, W., *et al.* Large-scale uniform bilayer graphene prepared by vacuum graphitization of 6H-SiC(0001) substrates. *J. Phys. Condens. Matter* **25**, 095002 (2013).

33. Zhang, Y., *et al.* Giant phonon-induced conductance in scanning tunnelling spectroscopy of gate-tunable graphene. *Nat. Phys.* **4**, 627-630 (2008).

Acknowledgments

The ARPES and thin film growth works at the Stanford Institute for Materials and Energy Sciences and Stanford University are supported by the Office of Basic Energy Sciences, Division of Materials Science and AFOSR Grant FA9550-14-1-0277 through the University of Washington. Research performed at ALS (thin film growth and ARPES) is supported by the Office of Basic Energy Sciences, US DOE under Contract No. DE-AC02-05CH11231. SSRL is supported by the Office of Basic Energy Sciences, US DOE under Contract No. DE-AC02-76SF00515. Scanned probe measurements were supported by the VdW Heterostructure program (KCWF16) (STM spectroscopy) funded by the Office of Basic Energy Sciences, US DOE under Contract No. DE-AC02-05CH11231, as well as by National Science Foundation award EFMA-1542741 (surface treatment and topographic characterization). Z. L. is supported by the National Natural Science Foundation of China (11227902). S. T. acknowledges the support by CPSF-CAS Joint Foundation for Excellent Postdoctoral Fellows. J. J. and C. C. H. acknowledge the support of the NRF, Korea (No. 2011-0030787 and No. 2017R1A2B2003928). H. R. and C. H. acknowledge the support from the NRF, Korea through Max Planck Korea/POSTECH Research Initiative (No. 2011-0031558) and Basic Science Research Program (No. 2015R1C1A1A01053065). A portion of the computational work was performed using the resources of the National Energy Research Scientific Computing Center (NERSC) supported by the U.S. Department of Energy, Office of Science, under Contract No. DE-AC02-05CH11231.

Author contributions

S. T., C. Z., S. K. M. and Z. X. S. proposed and designed the research. S. T. performed the MBE growth. S. T. and C. Z. carried out the ARPES measurements and analyzed the ARPES data with

help from J. J., H. R., S. K. M., M. H., D. L.. D. W., Z. P., H. T., S. K., M. M. U. and M. F. C. performed the STM measurements and analyzed STM data. C. J., M. C., B. M. and T. P. D. carried out the density functional calculations and provided theoretical support. S. T., S. K. M., D. W. and Z. X. S. wrote the manuscript with contributions and comments from all authors.

Additional information

Supplementary information is available in the online version of the paper. Reprints and permissions information is available online at www.nature.com/reprints.

Correspondence and requests for materials should be addressed to S. K. M. (SKMo@lbl.gov) and Z. X. S. (zxshen@stanford.edu).

Competing financial interests

The authors declare no competing financial interests

Fig. 1. **Topological phase transition in 1T'-WTe_2.** (a) Crystal structure of 1T'-WTe_2. The doubled period due to the spontaneous lattice distortion from 1T phase is indicated by the red rectangle. (b) Schematic diagram to show the bulk band evolution from a topologically trivial phase, to a non-trivial phase, and then to a bulk band opening due to SOC. Calculated band structures for WTe_2 to show the evolution from (c) 1T-WTe_2 along ΓY direction, (d) 1T'-WTe_2 without SOC, and (e) 1T'-WTe_2 with SOC. Red and blue dotted bands highlight the two bands involved in band inversion, which mainly contain the $5d_{z^2}$ and $5d_{xz}$ orbital contents, respectively. + and - signs denote the parity of the Bloch states at the Γ point.

Fig. 2. **Characterization of epitaxially grown 1T'-WTe_2 and overall electronic structure from ARPES.** (a) RHEED pattern of graphene substrate (top) and sub-monolayer 1T'-WTe_2 (bottom). (b) Core level spectra of 1T'-WTe_2. The inset is a close-up for the region marked by red dashed rectangle. (c) Atomically-resolved STM topographic image of 1T'-WTe_2. Blue and red dots represent W and Te atoms, respectively. (d) Brillouin zone of 1T'-WTe_2. Time reversal invariant momenta Γ, X, Y, R are labeled by black dots. (e) Fermi surface map of 1T'-WTe_2. The intensity is integrated within a ±10 meV window around E_F. There are three domains rotated with respect to each other by 120 degrees due to difference in the symmetry of the sample and the substrate. The measured data along the ΓY high symmetry direction is unavoidably mixed with the signals from the ΓP and ΓP' directions. The schematic contributions from different domains are represented by different color panes above the real Fermi surface map at the bottom. (f) Overall band structure measured along the experimental ΓY direction. (g) The second derivative spectra to enhance low intensity features. The overlaid black lines are the calculated band structure along the ΓY direction. (h) Calculated band structure along the ΓY (black) and ΓP/P' (red) directions, respectively. The low energy electronic structure around the Γ-point is dominated by the contributions from the ΓY bands.

406 **Fig. 3**. **Band gap opening in monolayer 1T'-WTe_2** (a) Calculated band structure along the ΓY
407 direction. (b) ARPES data along ΓY direction taken from surface K-doped sample. (c) EDCs for
408 the data in panel (b). (d) EDCs from the momentum positions marked with green and red lines in
409 (b). The green line corresponds to the conduction band bottom and the red line corresponds to
410 the valence band top. (e) Fermi surface map of K-doped sample. Six electron pockets are due to
411 the 3 rotational domains as explained for Fig. 2e. We only focus on the FS from a single domain.
412 (f) Stacking plot of cuts between the parallel dotted lines labeled in (g).
413

Fig. 4. **Tunneling spectroscopy in the bulk and at the edge of 1T'-WTe_2.** (a) STM dI/dV spectrum acquired in the bulk of monolayer 1T'-WTe_2. The inset is the high symmetry ARPES cut along the ΓY direction aligned in energy with the STS spectrum (acquired from a K-doped sample). Since the surface K-doping raises the position of E_F by 70meV, the whole ARPES spectrum is shifted by that amount for proper comparison with STS. (b) Representative dI/dV spectra taken at the edge (orange) and in the bulk (purple), respectively. (c) dI/dV spectra taken across the step edge of a 1T'-WTe_2 monolayer island (top), and corresponding height profile (bottom).

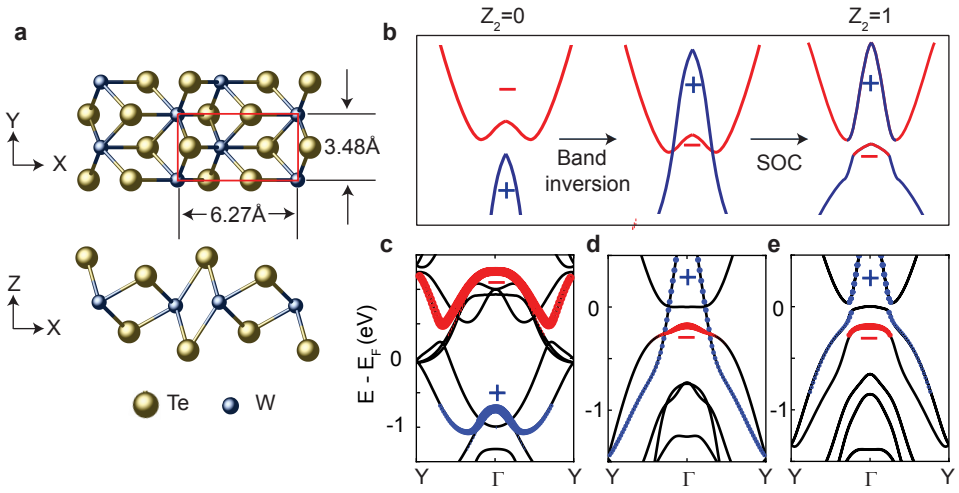
a
Y
X
3.48Å
6.27Å
Z
X
Te
W
b
Z2=0
Z2=1
Band
inversion
SOC
c
d
e
E - EF (eV)
0
-1
Y
Γ
Y

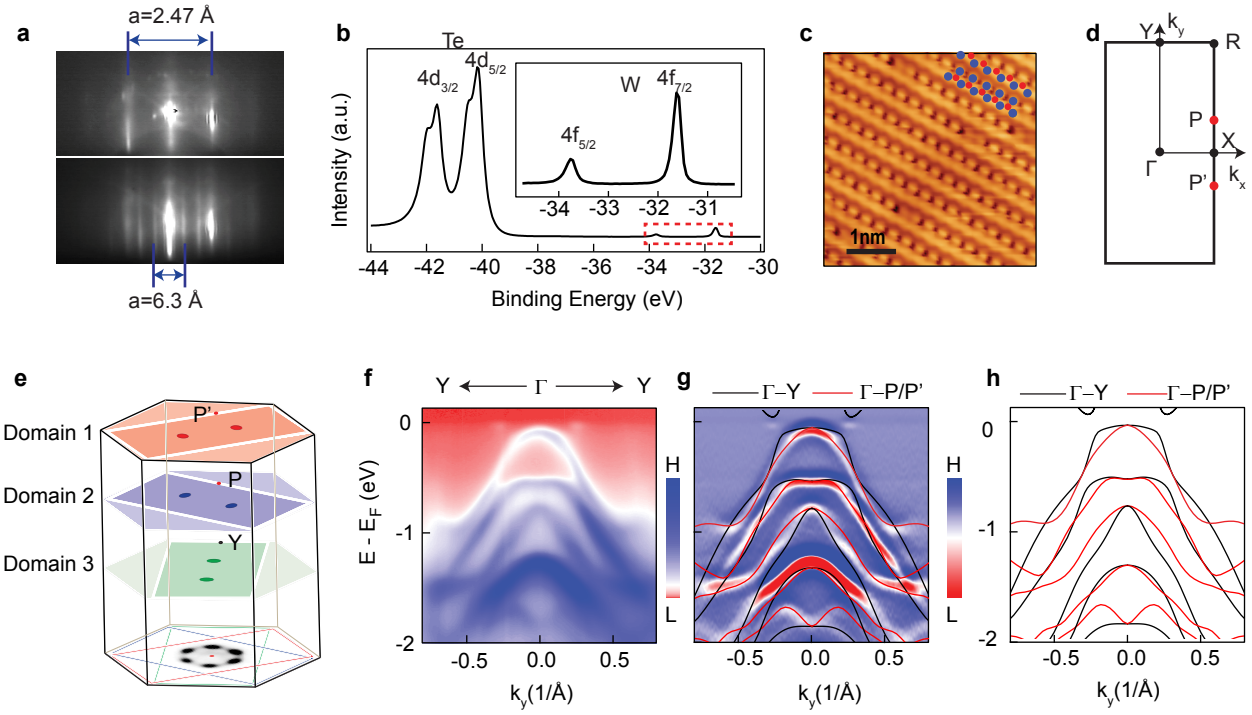
a
a=2.47 Å
a=6.3 Å
b
Te
4d3/2
4d5/2
W
4f7/2
4f5/2
Intensity (a.u.)
Binding Energy (eV)
c
1nm
d
Y
ky
R
P
X
Γ
P'
kx
e
Domain 1
Domain 2
Domain 3
P'
P
Y
f
Y ⟵ Γ ⟶ Y
E - EF (eV)
ky(1/Å)
H
L
g
Γ–Y
Γ–P/P'
ky(1/Å)
h
Γ–Y
Γ–P/P'
ky(1/Å)

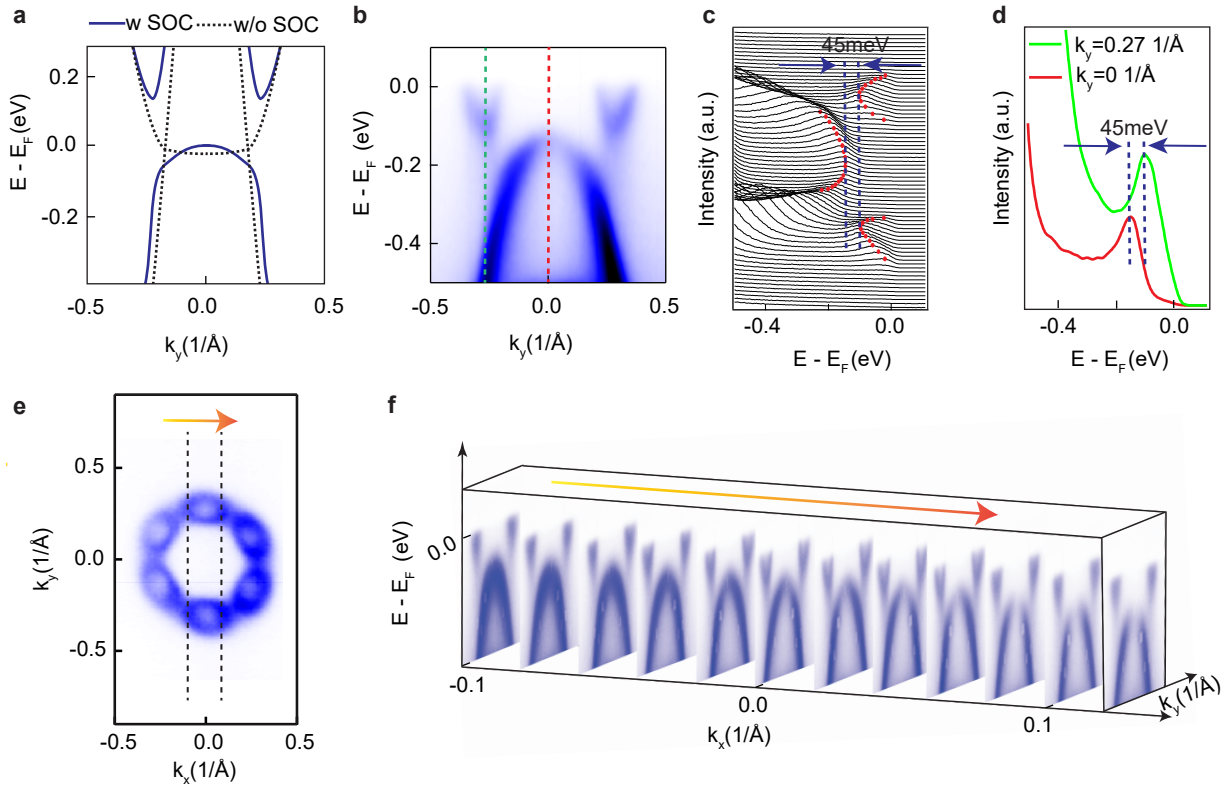
a
w SOC
w/o SOC
E - E_F (eV)
k_y(1/Å)
b
E - E_F (eV)
k_y(1/Å)
c
45meV
Intensity (a.u.)
E - E_F (eV)
d
k_y=0.27 1/Å
k_y=0 1/Å
45meV
Intensity (a.u.)
E - E_F (eV)
e
k_y(1/Å)
k_x(1/Å)
f
E - E_F (eV)
k_x(1/Å)
k_y(1/Å)

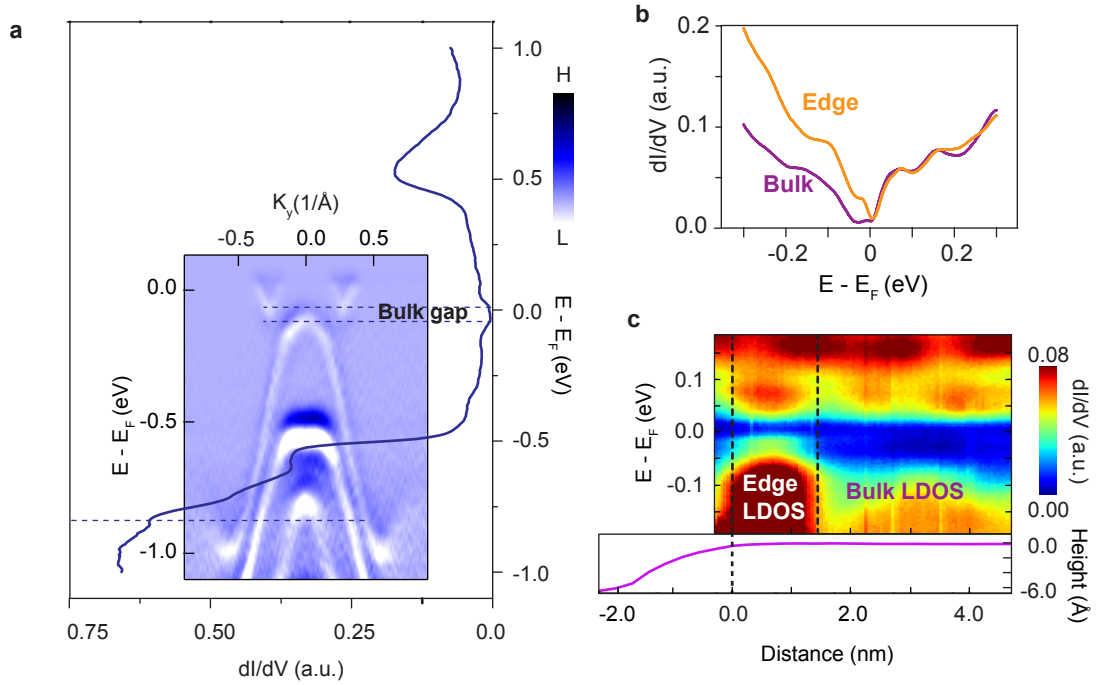
a
b
c
Bulk gap
K_y(1/Å)
E - E_F (eV)
dI/dV (a.u.)
H
L
Edge
Bulk
Edge LDOS
Bulk LDOS
Height (Å)
Distance (nm)